

Orbital torque in magnetic bilayers

Dongjoon Lee

Korea Institute of Science and Technology

Dongwook Go

Forschungszentrum Jülich

Hyeon-Jong Park

Korea University

Wonmin Jeong

Korea Institute of Science and Technology

Hye-Won Ko

Korea Advanced Institute of Science and Technology

Deokhyun Yun

Korea Institute of Science and Technology

Daegeun Jo

Pohang University of Science and Technology

Soogil Lee

Korea Advanced Institute of Science and Technology

Gyungchoon Go

Korea University <https://orcid.org/0000-0003-4586-8631>

Jung Hyun Oh

Korea University

Kab-Jin Kim

Korea Advanced Institute of Science and Technology <https://orcid.org/0000-0002-8378-3746>

Byong-Guk Park

KAIST <https://orcid.org/0000-0001-8813-7025>

Byoung-Chul Min

Korea Institute of Science and Technology (KIST) <https://orcid.org/0000-0001-8215-3286>

Hyun Cheol Koo

Korea Institute of Science and Technology <https://orcid.org/0000-0001-5044-1355>

Hyun-Woo Lee

Pohang University of Science and Technology <https://orcid.org/0000-0002-1648-8093>

OukJae Lee

Korea Institute of Science and Technology <https://orcid.org/0000-0001-9135-8347>

Kyung-Jin Lee (✉ kjlee@kaist.ac.kr)

Korea Advanced Institute of Science and Technology (KAIST) <https://orcid.org/0000-0001-6269-2266>

Article

Keywords: spintronics, magnetic bilayers, orbital Hall effect

Posted Date: May 19th, 2021

DOI: <https://doi.org/10.21203/rs.3.rs-509141/v1>

License:   This work is licensed under a Creative Commons Attribution 4.0 International License.

[Read Full License](#)

Version of Record: A version of this preprint was published at Nature Communications on November 18th, 2021. See the published version at <https://doi.org/10.1038/s41467-021-26650-9>.

Orbital torque in magnetic bilayers

Dongjoon Lee^{1,2†}, Dongwook Go^{3,4†}, Hyeon-Jong Park^{1†}, Wonmin Jeong^{2,5}, Hye-Won Ko⁶,
Deokhyun Yun^{2,7}, Daegeun Jo³, Soogil Lee⁸, Gyungchoon Go⁶, Jung Hyun Oh⁵, Kab-Jin Kim⁶,
Byong-Guk Park⁸, Byoung-Chul Min², Hyun Cheol Koo^{1,2}, Hyun-Woo Lee^{3,9★}, OukJae Lee^{2★},
and Kyung-Jin Lee^{6★}

¹KU-KIST Graduate School of Converging Science and Technology, Korea University, Seoul 02841, Korea

²Center for Spintronics, Korea Institute of Science and Technology, Seoul 02792, Korea

³Department of Physics, Pohang University of Science and Technology, Pohang 37673, Korea

⁴Basic Science Research Institute, Pohang University of Science and Technology, Pohang 37673, Korea

⁵Department of Materials Science and Engineering, Korea University, Seoul 02841, Korea

⁶Department of Physics, Korea Advanced Institute of Science and Technology, Daejeon 34141, Korea

⁷Department of Electrical Engineering, Korea University, Seoul 02841, Korea

⁸Department of Materials Science and Engineering, Korea Advanced Institute of Science and Technology, Daejeon 34141, Korea

⁹Asia Pacific Center for Theoretical Physics, Pohang 37673, Korea

†These authors equally contributed to this work.

★Correspondence to: hwl@postech.ac.kr (H.-W. Lee), ojlee@kist.re.kr (O. Lee),
kjlee@kaist.ac.kr (K.-J. Lee)

Abstract

The spin Hall effect describes an electric-field-induced generation of spin currents through spin-orbit coupling. Since the spin-orbit coupling alone cannot generate the angular momentum, there must be a more fundamental process of the spin Hall effect. Theories suggested that an electric-field-induced generation of orbital currents, called orbital Hall effect, is the fundamental process, and spin currents are subsequently converted from orbital currents. Despite its fundamental importance, the orbital Hall effect has not been confirmed experimentally. Motivated by a recent theoretical proposal of torque generation by orbital angular momentum injection, we examine the current-induced torque experimentally in various ferromagnet/heavy metal bilayers. We find that the net torque in Ni/Ta bilayers is opposite in sign to the spin Hall theory prediction but instead consistent with the orbital Hall theory, which confirms the orbital torque generated by the orbital Hall effect. It will invigorate researches on spin-orbit-coupled phenomena based on orbital engineering.

INTRODUCTION

The spin Hall effect (SHE)^{1,2,3} refers to an electrical generation of spin currents flowing in a transverse direction (or spin Hall current). It is often stated that the SHE originates from the spin-orbit coupling (SOC). This statement requires refinement, however, because the bare SOC $\left(\frac{e}{2m^2c^2}\right) \mathbf{S} \times \mathbf{p} \cdot \mathbf{E}$ between the electron spin \mathbf{S} and the momentum \mathbf{p} is many orders of magnitude too small to explain a spin Hall current generated by an external electric field \mathbf{E} ⁴. Instead a spin Hall current is generated through the atomic SOC⁵ ($\sim \alpha_{SOC} \mathbf{L} \cdot \mathbf{S}$), where the coefficient α_{SOC} parametrizes the strength of the electric field produced by *atomic nuclei* (instead of the externally applied electric field \mathbf{E}) and \mathbf{L} is the orbital angular momentum near the nuclei. Note that there is no coupling between \mathbf{E} and \mathbf{S} in the atomic SOC. The true $\mathbf{E} - \mathbf{S}$ coupling arises rather in two steps; \mathbf{E} couples to \mathbf{L} through non-SOC processes^{6,7} and \mathbf{L} couples to \mathbf{S} through the atomic SOC. This signifies the importance of the atomic orbital degree of freedom for the SHE.

Theories^{8,9,10,11} to understand the SHE are directed toward the intrinsic SHE, which does not resort to spin-dependent scattering caused by disorder. In systems with broken inversion symmetry, the intrinsic SHE is often described⁹ by the coupling between the electron's crystal momentum \mathbf{k} and \mathbf{S} , which is responsible for spin-dependent level splitting. In such description, \mathbf{L} does not appear explicitly so that the role of the orbital degree of freedom in the SHE is concealed. The essential necessity of the orbital degree of freedom for the SHE becomes evident in centrosymmetric systems^{10,11}, where the $\mathbf{k} - \mathbf{S}$ coupling is forbidden by the inversion and time-reversal symmetries so that the previous description without \mathbf{L} fails to describe the intrinsic SHE. To understand the intrinsic SHE properly, the orbital degree of freedom needs to be explicitly taken care of. The multi-orbital tight-binding studies^{10,11} of *4d*

and $5d$ transition metals revealed that the SHE is not fundamental but is a concomitant effect of a more fundamental effect, the orbital Hall effect (OHE)¹², which refers to the electrical generation of a transverse flow of the orbital angular momentum (or orbital Hall current). Although the role of orbital angular momentum in the SHE has been ignored for a long time, it is actually a natural result of the angular momentum flow in solids¹³; the fundamental source of the angular momentum is the lattice, and the lattice angular momentum is transferred first to \mathbf{L} through the crystal-field potential and then to \mathbf{S} through the atomic SOC.

As a consequence of this causal relation between the fundamental OHE and the concomitant SHE, it was predicted that the spin Hall conductivity σ_{SH}^{NM} of a NM should be proportional to its orbital Hall conductivity σ_{OH}^{NM} times its spin-orbit correlation $R_{NM} = \langle \mathbf{L} \cdot \mathbf{S} \rangle_{NM}$. Since the calculated σ_{OH}^{NM} is positive for all examined $4d$ and $5d$ heavy metals whereas R_{NM} changes its sign from negative to positive as the outermost d shell of the heavy metals is progressively filled^{10, 11}, the relation between the OHE and the SHE predicts σ_{SH}^{NM} to exhibit a similar sign change as the outermost d shell is filled (Hund's rule type behaviour; Fig. 1A). Such sign change is consistent with experimental values of σ_{SH}^{NM} ^{14, 15}. A later theoretical study⁷ reported that the causal relation between the OHE and the SHE is not limited to $4d$ and $5d$ heavy metals but is more generic.

Experimental confirmation^{2, 3} of the SHE took several decades after the theoretical proposal¹ because experiments attempted to probe the SHE-induced spin accumulation, which is small. This phenomenon of a pure scientific curiosity soon gained wider attention after it was recognized that the injection of a spin Hall current into a ferromagnet (FM) generates a torque, called spin-orbit torque (SOT), which makes it much easier to detect and even manipulate the magnetization of the FM efficiently^{16, 17, 18, 19}. The SOT has been studied

extensively for FM/NM bilayers. Large SOT is of immense technological relevance and has been pursued mostly with $5d$ heavy metals such as Pt^{16, 18, 19} and Ta^{17, 20} chosen as the NM since they exhibit strong intrinsic SHE. On the other hand, the OHE has not been experimentally verified yet despite its fundamental importance. Interestingly, some of us recently predicted²¹ that the OHE can generate a torque (orbital torque) when an orbital Hall current is injected into a FM. This prediction provides a way to experimentally detect the OHE. Recent experiments on surface-oxidized Cu/ferromagnet structures converged to an idea that the orbital angular momentum is in action for the SOT^{22, 23, 24}, which is generated from the interfacial orbital Rashba state²⁵. Here, a contribution of the spin current is expected to be negligible due to negligible SOC of Cu. In general, however, both spin current and orbital current generate the torque on the magnetization, and thus it is crucial to devise an experimental protocol to unambiguously verify the presence of the orbital current in a situation where the spin current contribution to the SOT cannot be ignored.

RESULTS

Detection scheme of the orbital Hall effect

It is not simple to distinguish the orbital torque from the conventional SOT (arising from the spin Hall current injection) since the orbital torque and the SOT have identical properties with regard to all symmetry transformations such as time reversal, space inversion, and mirrors. However, the two torques depend on the spin-orbit correlations in a NM and a FM in different ways. Thus observation of such difference can constitute an experimental confirmation of the OHE. Figure 1B illustrates two channels that give rise to the two torques. The OHE is the initial

process for both channels: An electric field creates an orbital current J_L in a NM through the OHE. In the first channel, the orbital current J_L is converted to the spin current J_S within the NM through the SOC of the NM. This spin current is then injected into a FM and produces a conventional SOT. The sign of the resulting SOT is determined by the sign of σ_{SH}^{NM} ($\sim R_{NM}\sigma_{OH}^{NM}$). On the other hand, the second channel corresponds to the orbital torque: The orbital current J_L is injected into the FM. Within the FM, this orbital current J_L is then converted to the spin current J_S through the SOC of the FM and exerts a torque. For the second channel, the sign of orbital torque is determined by the sign product of the orbital Hall conductivity of the NM (σ_{OH}^{NM}) and the effective spin-orbit correlation C_{FM} in the FM. Here, C_{FM} describes how much spin accumulation is induced in the FM in response to an orbital Hall current injected from the NM (see section S1). The sign of C_{FM} is essentially the same with that of the FM's spin-orbit correlation $R_{FM} = \langle \mathbf{L} \cdot \mathbf{S} \rangle_{FM}$, and its magnitude is roughly proportional to R_{FM} that corresponds to the orbital-to-spin conversion for an internally generated orbital Hall current within the FM. Thus the net SOT of FM/NM bilayer consists of not only a spin Hall contribution proportional to σ_{SH}^{NM} but also an additional orbital Hall contribution proportional to $C_{FM}\sigma_{OH}^{NM}$.

Given these two contributions, there are three possible cases for the sign of the net SOT (conventional SOT + orbital torque): (i) When $\sigma_{SH}^{NM} \cdot C_{FM}\sigma_{OH}^{NM} > 0$, both channels generate torques with the same sign so that the OHE effectively strengthens the SHE. (ii) When $\sigma_{SH}^{NM} \cdot C_{FM}\sigma_{OH}^{NM} < 0$ and the spin Hall contribution is larger in magnitude than the orbital Hall one, the sign of net SOT is determined by the sign of σ_{SH}^{NM} and the OHE effectively weakens the SHE. (iii) When $\sigma_{SH}^{NM} \cdot C_{FM}\sigma_{OH}^{NM} < 0$ and the spin Hall contribution is smaller in magnitude than the orbital Hall one, the sign of the net SOT is opposite to that expected from the sign of

σ_{SH}^{NM} . For the cases (i) and (ii), distinguishing the OHE from the SHE is difficult because it requires a detailed quantitative analysis of the magnitudes of each contribution, which is often ambiguous. For the case (iii), however, the sign reversal of net SOT by the OHE is unique and unambiguous. Thus if the sign reversal in the case (iii) is realized in experiments, it convincingly supports the presence of the OHE and the associated orbital torque.

To check whether or not the case (iii) can be realized in real materials, we compute σ_{SH}^{NM} and σ_{OH}^{NM} of NMs (Pt and Ta), and C_{FM} of FMs (Fe, CoFe, Co, and Ni), based on a first-principles calculation (see section S1). Using the signs and magnitudes of calculated σ_{SH}^{NM} , σ_{OH}^{NM} , and C_{FM} , we attempt to find out which combination of NM and FM would be most probable to realize the case (iii).

Figure 2 summarizes the calculation results. We find that for Pt, σ_{SH}^{Pt} and σ_{OH}^{Pt} are both positive and comparable in magnitude, whereas for Ta, σ_{SH}^{Ta} and σ_{OH}^{Ta} have the opposite signs and σ_{OH}^{Ta} is an order of magnitude larger than σ_{SH}^{Ta} (Fig. 2A). Thus the case (iii) can be more easily realized in Ta than in Pt. The calculated σ_{SH}^{NM} and σ_{OH}^{NM} are consistent with previous tight-binding^{10, 11} and first-principles^{26, 27} results. We also find that C_{FM} is positive for all of Fe, Co, and Ni (Fig. 2B), and increases with the atomic number or the number of $3d$ electrons (thus, a Hund-rule type behaviour). C_{FM} of CoFe is close to the average of C_{FM} values for Co and Fe. This FM-dependence of C_{FM} implies that the orbital torque should be most pronounced in Ni, which is also consistent with Ni's having the strongest spin-orbit correlation R_{FM} among the FM materials (see section S1).

Figure 2C and 2D respectively show $\sigma_{net}^{FM/NM}$ ($= \sigma_{SH}^{NM} + C_{FM}\sigma_{OH}^{NM}$) for FM/Pt and FM/Ta bilayers, calculated from the results in Fig. 2a-b. The signs of $\sigma_{net}^{FM/NM}$ for FM/Pt bilayers are

all positive, consistent with the sign of σ_{SH}^{Pt} . The signs of $\sigma_{net}^{FM/NM}$ for Fe/Ta, Co/Ta, and CoFe/Ta bilayers are all negative, consistent with the sign of σ_{SH}^{Ta} . However, the sign of $\sigma_{net}^{FM/NM}$ for Ni/Ta bilayer is positive and thus is the opposite to that expected for the sign of σ_{SH}^{Ta} , because $\sigma_{SH}^{Ta} \cdot C_{Ni} \sigma_{OH}^{Ta} < 0$ and $|\sigma_{SH}^{Ta}| < |C_{Ni} \sigma_{OH}^{Ta}|$ for this bilayer. This calculation suggests that the Ni/Ta bilayer is the most probable system to realize the case (iii), which motivates us to experimentally measure the sign of the net SOT for various FM/NM bilayers, including the Ni/Ta bilayer.

Experimental test of orbital torque

We first measure the net SOT from four types of bilayers: $\text{Co}_{40}\text{Fe}_{40}\text{B}_{20}(t_{FM})/\text{Pt}(5)$, $\text{Co}_{40}\text{Fe}_{40}\text{B}_{20}(t_{FM})/\text{Ta}(4)$, $\text{Ni}(t_{FM})/\text{Pt}(5)$, and $\text{Ni}(t_{FM})/\text{Ta}(4)$ (the numbers are in nanometers and t_{FM} is the FM thickness). The resistivity of Ta is $\sim 200 \mu\Omega \cdot \text{cm}$, and thus it is β -phase. The FM layer is passivated with Ta(2)/MgO(2) capping layers unless specified otherwise (see Materials and Methods). For the net SOT measurement, we use the spin-torque ferromagnetic resonance (ST-FMR) technique^{28,29,30,31,32} (see Materials and Methods), which is an established method to separately measure the damping-like torque (DLT) [$\tau_{DL} \propto \hat{\mathbf{m}} \times (\hat{\mathbf{m}} \times \hat{\mathbf{y}})$] and field-like torque (FLT) [$\tau_{FL} \propto (\hat{\mathbf{m}} \times \hat{\mathbf{y}})$] components of the SOT, where $\hat{\mathbf{m}}$ is the unit vector along the magnetization direction and $\hat{\mathbf{y}}$ is the direction perpendicular to both directions of current flow ($\hat{\mathbf{x}}$) and thickness ($\hat{\mathbf{z}}$). From the measured results, we focus only on the sign of the DLT because it reflects the signs of the spin Hall and orbital Hall conductivities.

For the ST-FMR measurement (Fig. 3A), a radio frequency (RF) current injected into a FM/NM bilayer generates oscillating SOTs, which in turn excites the magnetization precession

at resonance. This magnetization precession induces a net oscillation in the magnetoresistance. Combined with the applied RF current, the resistance oscillation induces a finite DC voltage V_{mix} as a function of the applied magnetic field H , given as²⁸

$$V_{mix}(H) = V_S \frac{\Delta H^2}{(H-H_{res})^2 + (\Delta H)^2} + V_A \frac{(H-H_{res})\Delta H}{(H-H_{res})^2 + (\Delta H)^2}, \quad (1)$$

where V_S (V_A) is the symmetric (antisymmetric) term of resonance amplitude, H_{res} is the resonance field, and ΔH is the half linewidth at the half maximum. The V_S corresponds to the DLT, whereas the V_A corresponds to the sum of the FLT and current-induced Oersted field torque.

Figures 3B-E show representative ST-FMR data of four bilayers ($t_{FM} = 5$ nm). The CoFeB/Pt bilayer (Fig. 3B) shows a negative V_S corresponding to a positive spin Hall angle that has the same sign with σ_{SH}^{Pt} , whereas the CoFeB/Ta bilayer (Fig. 3C) shows a positive V_S corresponding to a negative spin Hall angle that has the same sign as σ_{SH}^{Ta} . The Ni/Pt bilayer (Fig. 3D) shows a negative V_S , same as for the CoFeB/Pt bilayer, which is consistent with the sign of σ_{SH}^{Pt} . However, we observe the abnormal case for the Ni/Ta bilayer: this bilayer shows a negative V_S (Fig. 3E), which is the opposite to that expected from the sign of σ_{SH}^{Ta} .

The abnormal DLT sign of Ni/Ta bilayer is further confirmed by the FM thickness (t_{FM}) dependence of V_{mix} (see section S2), which gives t_{FM} -independent DLT and FLT efficiencies. We perform ST-FMR measurements for various t_{FM} and obtain the quantity ξ_{FMR} , defined from V_S/V_A ^{29,30},

$$\xi_{FMR} = \frac{V_S}{V_A} \left(\frac{e}{\hbar} \right) 4\pi M_s t_{FM} t_{NM} \sqrt{1 + \frac{4\pi M_{eff}}{H_{res}}}, \quad (2)$$

where M_s is the saturation magnetization of FM, t_{NM} is the thickness of NM (Pt or Ta), and $4\pi M_{eff}$ is the out-of-plane demagnetization field (see Materials and Methods). The measurement of ξ_{FMR} as a function of t_{FM} allows us to separately estimate the damping-like (ξ_{DL}) and field-like (ξ_{FL}) torque efficiencies, using^{29, 30, 33} (see Materials and Methods)

$$\frac{1}{\xi_{FMR}} = \frac{1}{\xi_{DL}} \left(1 + \frac{\hbar}{e} \frac{\xi_{FL}}{4\pi M_s t_{FM} t_{NM}} \right). \quad (3)$$

Equation (3) shows that the intercept of $1/\xi_{FMR}$ in the limit of $1/t_{FM} \rightarrow 0$ gives the sign of ξ_{DL} . As shown in Figs. 3F (CoFeB/Pt and CoFeB/Ta) and 3G (Ni/Pt and Ni/Ta) (see section S2), the signs of the intercepts, indicated by arrows, are all consistent with those of the symmetric peaks in Figs. 2B-E. Thus, the abnormal sign of the DLT for the Ni/Ta bilayer is not specific to a sample but general. As independent tests, we also experimentally examine the sign of the DLT by measuring the linewidth (or effective damping) modulation by a DC current (see section S3), and by utilizing the 2nd harmonic Hall measurement for the in-plane magnetized systems (see section S4). We obtain a consistent result with ST-FMR. Therefore, it is clear that the DLT sign of the Ni/Ta bilayer is opposite to that expected from the sign of σ_{SH}^{Ta} . We note that this abnormal sign is consistent with the above-explained case (iii), i.e., the orbital torque. It is also found that the measured Landé g-factors for Ni/Pt, Ni/Ta, CoFeB/Pt and CoFeB/Ta are consistent with the OHE scenario (section S5). Figure 3H (3I) summarizes the effective spin-Hall angle (spin Hall conductivity) for various bilayers (FM = FeB, CoFeB, Co, Ni, NM = Pt, Ta; see section S6 for further details). Note that the material-dependent variation of the effective spin Hall conductivity is in qualitative agreement with the theoretical result in Figs. 2C and 2D, which supports the OHE theory.

Other possible mechanisms of the abnormal DLT sign

In the previous section, our analysis focuses on the competition between the SHE and OHE for the current-induced torque, but neglects other mechanisms. To examine the effects of different mechanisms, we perform control experiments.

In addition to the bulk SHE of NM, recent studies suggested an important role of the interfacial SOC in the SOT^{34, 35, 36}. As the sign of the spin polarization carried by interface-generated spin currents can be different from that of the bulk SHE of NM, we investigate the interfacial SOC effect at both interfaces of Ni/Ta bilayer: Ni/Ta interface and MgO/Ni interface. To check if the Ni/Ta interface is crucial, we carry out ST-FMR measurements for Ni(7)/Cu(t_{Cu})/Ta(4) samples where a Cu layer is inserted between Ni and Ta layers. We find that the DLT still has the same abnormal sign (Fig. 4A, B; see section S2). The sign of DLT is maintained regardless of t_{Ni} for Ni(t_{Ni})/Cu(1)/Ta(4) layers (see section S2). We also perform ST-FMR measurements for Ni(7)/Ti(0.5-3)/Ta(4) and for Ni(t_{Ni})/Ti(1)/Ta(4), and find that the sign of the DLT is still abnormal. These results imply that the interfacial SOC effect³⁷ from the Ni/Ta interface is not responsible for the abnormal sign. The MgO/Ni interface may also affect the sign of the DLT because the oxide layer is known to enhance the Rashba effect at the interface^{38, 39}. To check this possibility, we replace Ta(2)/MgO(2) capping layers with HfO_x(3). In the resulting HfO_x/Ni interface, the interaction between Ni and oxygen is expected to be strongly suppressed since the enthalpy of formation (≈ -1120 kJ/mol) of HfO_x is much larger in magnitude than that of MgO (≈ -600 kJ/mol)⁴⁰. We find that the sign of the DLT does not change with this replacement (Fig. 4C, D; see section S2), implying that the MgO/Ni interface is not crucial either. These control experiments allow us to exclude the possibility that the abnormal sign is caused by the interfacial effect.

Another possible contribution can be driven by a self-induced spin accumulation of the FM, which is known as the anomalous torque^{41, 42}. A recent first-principles calculation suggests that the anomalous torque can be substantial in Ni due to its pronounced spin-orbit correlation, which also contributes to the abnormal sign of the SOT due to a positive sign of σ_{SH}^{Ni} ⁴³. To estimate such contribution, we perform ST-FMR measurements for Ni(t_{Ni})/Cu(5) bilayers (Figs. 4E, F). Since both OHE and SHE are negligible in pure Cu⁴⁴, the SOT in Ni/Cu represents a contribution from the anomalous torque. While the signs are still abnormal as expected, the magnitudes of the SOT are an order of magnitude smaller than that in Ni/Ta. Combining all these results with those shown in Figs. 3 and 4, we conclude that the abnormal sign of DLT for the Ni/Ta layer originates from the orbital torque, which in turn proves the existence of the OHE.

DISCUSSION

The orbital degree of freedom is a recurring theme in condensed matter physics. It is now well established that the giant tunnelling magnetoresistance in MgO-based magnetic tunnel junction^{45, 46} is due to the orbital-dependent tunnelling^{47, 48}. Moreover, it is known that the theoretical limit of magnetic anisotropy⁴⁹ and the large Rashba spin splitting^{6, 50} can be achieved by utilizing the orbital degree of freedom. In this respect, our experimental confirmation of the orbital torque and the OHE has a number of important implications. Whereas previous attempts to strengthen the SHE are based on a material search for NM materials with strong SOC, the relation $\sigma_{SH}^{NM} \propto \sigma_{OH}^{NM} R_{NM}$ suggests that large σ_{SH}^{NM} may be achieved alternatively by strengthening σ_{OH}^{NM} instead. Theoretical studies of single-element materials report large σ_{OH}^{NM} of the order of $10^4 (\hbar/e)(\Omega \cdot \text{cm})^{-1}$ for various materials^{7, 10, 11}

but this value may be enhanced further, for instance, in multi-element materials by optimizing the orbital degree of freedom. For device applications based on the current-induced torque, another interesting direction is to pursue strengthening the orbital torque by optimizing the FM material choice, since the orbital torque can be strengthened in FM with strong SOC⁷. Considering that the weak SOC material Ni can already overcome the strong SHE of Ta and reverse the net SOT sign in a Ni/Ta bilayer, this is a promising direction to pursue enhancing the torque. It thus provides a new opportunity that was not explored by present trends to optimize the NM material choice. By the way, our experiment intentionally uses well-characterized 3*d* FMs with weak SOC to avoid possible complications by strong SOC in FMs since our work is aimed to confirm the OHE unambiguously instead of maximizing the orbital torque. To maximize the total torque, it is actually desired to choose NM and FM materials so that the orbital torque and the conventional SOT have the same sign to add them up instead of cancelling each other. We expect that the orbital current confirmed in this experiment opens a new avenue of exciting opportunities for more advanced spintronic and possibly orbitronic devices. Moreover, our result suggests that the orbital engineering is an efficient pathway to enhance the spin current that is an essential ingredient not only in spintronics but also in various branches of condensed matter physics.

MATERIALS AND METHODS

Thin film growth and characterization. The multilayer films were prepared on thermally oxidized Si substrates by DC/RF magnetron sputtering at room temperature. The multilayers

consist of capping layer / ferromagnetic-metal (FM) / non-magnetic-metal (NM) / substrate. The combinations of the FM and NM were $\text{Co}_{40}\text{Fe}_{40}\text{B}_{20}(t_{\text{CoFeB}})/\text{Pt}(5)$, $\text{Co}_{40}\text{Fe}_{40}\text{B}_{20}(t_{\text{CoFeB}})/\text{Ta}(4)$, $\text{Ni}(t_{\text{Ni}})/\text{Pt}(5)$, and $\text{Ni}(t_{\text{Ni}})/\text{Ta}(4)$ (nominal thickness in nm). The t_{CoFeB} was varied from 2 to 10 nm and t_{Ni} from 3 to 15 nm. The capping layer was either $\text{Ta}(2)/\text{MgO}(2)$ or $\text{HfO}_x(3)$ to protect its underlayers. The base pressure of the chamber was maintained less than 5×10^{-8} Torr, and the deposition rates were kept lower than 0.5 Å/s. A vibrating sample magnetometer (VSM) was used to measure the saturation magnetization (M_s).

ST-FMR Device fabrication and measurement. To prepare devices for the ST-FMR measurement, we used optical lithography and ion-milling to pattern the multilayer films into rectangular strips with 15 μm -width (w) and 50 μm -length (l). In a subsequent process, a waveguide contact made of Au (100 nm)/ Ti (10 nm) was defined on top of the samples to apply a microwave current to the devices. The samples were not exposed to high temperature (> 120 °C) during the fabrication process as no post-annealing was carried out. All the measurements were performed at room temperature. For ST-FMR measurement, a pulsed microwave signal in the range 4–14 GHz with a nominal output power of 10-20 dBm was applied to the samples. An in-plane external magnetic field (from -1.8 kOe to +1.8 kOe) was swept at an angle of 45°. The V_{mix} was simultaneously detected with a lock-in amplifier connected to the DC port of the bias tee. By fitting $V_{\text{mix}}(H)$ with equation (1), we obtained H_{res} , ΔH , V_S , and V_A at different frequencies for each sample. The center frequency of the resonance peak (f) follows the Kittel equation, $f = (\gamma/2\pi)\sqrt{H_{\text{res}}(H_{\text{res}} + 4\pi M_{\text{eff}})}$, where γ is the gyromagnetic ratio and $4\pi M_{\text{eff}}$ was extracted from a fit to the Kittel equation.

ST-FMR data analysis. In Eq. (1), V_S is proportional to the DLT (τ_{DL}), whereas V_A originates from the sum of FLT (τ_{FL}) and Oersted field torque (τ_{Oe});

$$V_S \propto \gamma \tau_{DL} = \gamma \frac{\hbar}{2e} \frac{J_{NM}}{4\pi M_s t_{FM}} \xi_{DL}, \quad (4)$$

$$V_A \propto \gamma (\tau_{Oe} + \tau_{FL}) \sqrt{1 + \frac{4\pi M_{eff}}{H_{res}}} \approx \gamma \left(\frac{t_{NM} J_{NM}}{2} + \frac{\hbar}{2e} \frac{J_{NM}}{4\pi M_s t_{FM}} \xi_{FL} \right) \sqrt{1 + \frac{4\pi M_{eff}}{H_{res}}}, \quad (5)$$

where \hbar is the Planck's constant, e is the electron charge, J_{NM} is the current density through the NM, and t_{NM} is the thickness of NM. The measured voltages are interpreted to magnetic precession angles of less than 0.5° , corresponding to a linear-response regime. Thus we ignored the contribution in V_S from spin-pumping and inverse SHE^{32, 51}, which are estimated to be less than $0.2 \mu\text{V}$. We also measured the magnetic dead layer thickness from M_S versus t_{FM} , but found that it does not affect the sign and even magnitude of the DLT. The V_{mix} usually includes a field (H)-independent offset, which was eliminated in all data.

SUPPLEMENTARY MATERIALS

Supplementary material for this article is available at ...

section S1. First-principles calculation

section S2. FM-thickness dependence of ST-FMR signals

section S3. Linewidth (ΔH) modulation by a DC current

section S4. In-plane 2nd harmonic Hall measurements

section S5. Discussion on the SOC in 3d-FM

section S6. Overall trends of the SOT variation

fig. S1. Comparison between $\langle \delta S_x \rangle$ and $\langle \delta S_x \rangle^{\text{OT,bulk}}$.

fig. S2. Spin-orbit correlation $R_{FM} = \langle L \cdot S \rangle_{FM}$ for various FMs (Co, Fe, CoFe, and Ni).

fig. S3. $V_{mix}(H)$ of Ni(t_{Ni})/Pt bilayers.

fig. S4. $V_{mix}(H)$ of Ni(t_{Ni})/Ta bilayers.

fig. S5. $V_{mix}(H)$ of Ni(7)/Cu(t_{Cu})/Ta layers.

fig. S6. $V_{mix}(H)$ of Ni(t_{Ni})/Cu(1)/Ta layers.

fig. S7. $V_{mix}(H)$ of HfO_x/Ni(t_{Ni})/Pt layers.

fig. S8. $V_{mix}(H)$ of HfO_x/Ni(t_{Ni})/Ta layers.

fig. S9. Linewidth (ΔH) modulation by a DC current.

fig. S10. $R_H^{2\omega}(\varphi)$ of FM/NM layers.

fig. S11. $R_H^\omega(H_z)$ of FM/NM layers.

fig. S12. Estimation of SOTs from 2nd harmonic Hall measurements.

fig. S13. Evaluated Landé g-factors

fig. S14. Trend of SOT for various FM/NM layers

Acknowledgements

We acknowledge M. D. Stiles for discussion. D.G. acknowledges discussions with Yuriy Mokrousov, Jan-Philipp Hanke, and Frank Freimuth. D.L., H.J.P., H.W.K., G.G., J.H.O. and K.-J.L. were supported by the National Research Foundation of Korea (NRF-2020R1A2C3013302 & 2020M3F3A2A01082591). D.L., H.J.P., and H.W.K. were supported by the KU-KIST school project. D.L., W.J., D.Y., B.C.M., H.C.K., and O.L. were supported by the National Research Council of Science & Technology (NST) grant (No. CAP-16-01-KIST), the KIST Institutional Program (2E29410) and Institute of Information & communications Technology Planning & Evaluation (IITP) grant funded by the Korea government (MSIT) (No. 2019-0-00296). D.G., D.J., and H.-W.L. were supported by the Samsung Science and Technology Foundation (BA-1501-07 & BA-1501-51).

Author contributions

D.L., D.G., and H.J.P. equally contributed to this work. H.W.L., O.L. and K.J.L. supervised the study. D.L. and W.J. prepared films/devices and performed ST-FMR measurements with help from D.Y., B.C.M., H.C.K., and O.L. D.G., H.J.P., H.W.K., and D.J. carried out theoretical calculations with help from G.G., J.H.O., H.W.L., and K.J.L. D.L., O.L., and K.J.L. analysed the results with help from H.W.L., S.L., B.G.P., and K.J.K. K.J.L., O.L., H.W.L., and H.C.K. wrote the manuscript. All authors discussed the results and commented on the manuscript.

Competing interests

The authors declare that they have no competing interests.

Data and materials availability

All data needed to evaluate the conclusions in the paper are present in the paper and/or the Supplementary Materials. Additional data related to this paper may be requested from the authors.

Figure legends

Fig. 1. Schematic Illustration of the OHE and orbital torque. (A) When an electric field is applied along the horizontal direction, a transverse orbital current is generated owing to the OHE. This orbital current is converted to a spin current through the spin-orbit coupling. Depending on the sign of spin-orbit correlation $R = \langle \mathbf{L} \cdot \mathbf{S} \rangle$, the spin polarization of the resulting spin current is either parallel (left panel) or antiparallel (right panel) to the orbital polarization of the orbital current. (B) Two channels for generating the torque in FM/NM bilayers. The first channel: An orbital current J_L created through the OHE is converted to a spin current J_S within the NM. For a negative spin-orbit correlation of NM ($R_{NM} < 0$), the direction of spin polarization carried by J_S is the opposite to that of the orbital polarization carried by J_L , which is the case of Ta. This spin current is injected into a FM and exerts a torque on the magnetization $\hat{\mathbf{m}}$. The second channel: J_L created through the OHE in the NM is injected into a FM in which J_L is converted to J_S . This J_S exerts a torque on $\hat{\mathbf{m}}$, which we call the orbital torque. For FMs with a positive orbital-to-spin conversion efficiency of FM C_{FM} (such as Fe, Co, CoFe, and Ni), the direction of the spin polarization carried by J_S is the same with that of the orbital polarization carried by J_L . When the second channel supplies a stronger torque than the first channel and the contributions from the two channels have the opposite signs, the sign of the net torque is the opposite to that expected for the spin Hall effect of NM.

Fig. 2. First-principles results. (A) Spin Hall conductivity σ_{SH}^{NM} and orbital Hall conductivity σ_{OH}^{NM} of Pt and β -Ta. (B) Orbital-to-spin conversion efficiency C_{FM} of Fe, CoFe, Co, and Ni. (C), $\sigma_{SH}^{NM} + C_{FM}\sigma_{OH}^{NM}$ of FM/Pt bilayers (FM = Fe, Co, CoFe, and Ni). (D), $\sigma_{SH}^{NM} + C_{FM}\sigma_{OH}^{NM}$ of FM/Ta bilayers (FM = Fe, Co, CoFe, and Ni). In (B), the value of C_{FM} depends on the ratio T_L/T_S , where the spin (orbital) transparency T_S (T_L) denotes the likelihood of spin (orbital) Hall current gets transmitted through the FM/NM interface. The ratio T_L/T_S is assumed to be 0.3 in Fig. 2B, considering that the orbital relaxation is expected to be faster than the spin relaxation.

Fig. 3. ST-FMR results of FM/NM bilayers (FM = CoFeB, Ni, NM = Pt, Ta). (A) A schematic illustration of ST-FMR measurement. (B to E) $V_{mix}(H)$ of (B) CoFeB(5)/Pt, (C) CoFeB(5)/Ta, (D) Ni(5)/Pt, and (E) Ni(5)/Ta bilayers. Symbols are experimental results and lines are fitting results with Eq. (1). (F, G), $1/\xi_{FMR}$ as a function of $1/t_{FM}$ of (F) CoFeB(t_{CoFeB})/NM and (G) Ni(t_{Ni})/NM (NM = Pt, Ta). (H) The damping-like torque efficiency ξ_{DL} for various bilayers (FM = FeB, CoFeB, Co, Ni, NM = Pt, Ta). (I) The effective spin Hall conductivity (σ_{DL}) for various bilayers.

Fig. 4. Control experiments for other possible mechanisms. (A) ST-FMR spectra of a Ni(7)/Cu(3)/Ta sample. (B) ξ_{FMR} as a function of the Cu-layer thickness t_{Cu} for Ni(7)/Cu(t_{Cu})/Ta samples. (C) ST-FMR spectra of a HfO_x(3)/Ni(10)/Ta sample. (D) $1/\xi_{FMR}$ as a function of $1/t_{Ni}$ of HfO_x(3)/Ni(t_{Ni})/Ta samples. (E) ST-FMR spectra of a Ni(7)/Cu(5) sample. (F) $1/\xi_{FMR}$ as a function of $1/t_{Ni}$ of Ni(t_{Ni})/Cu samples.

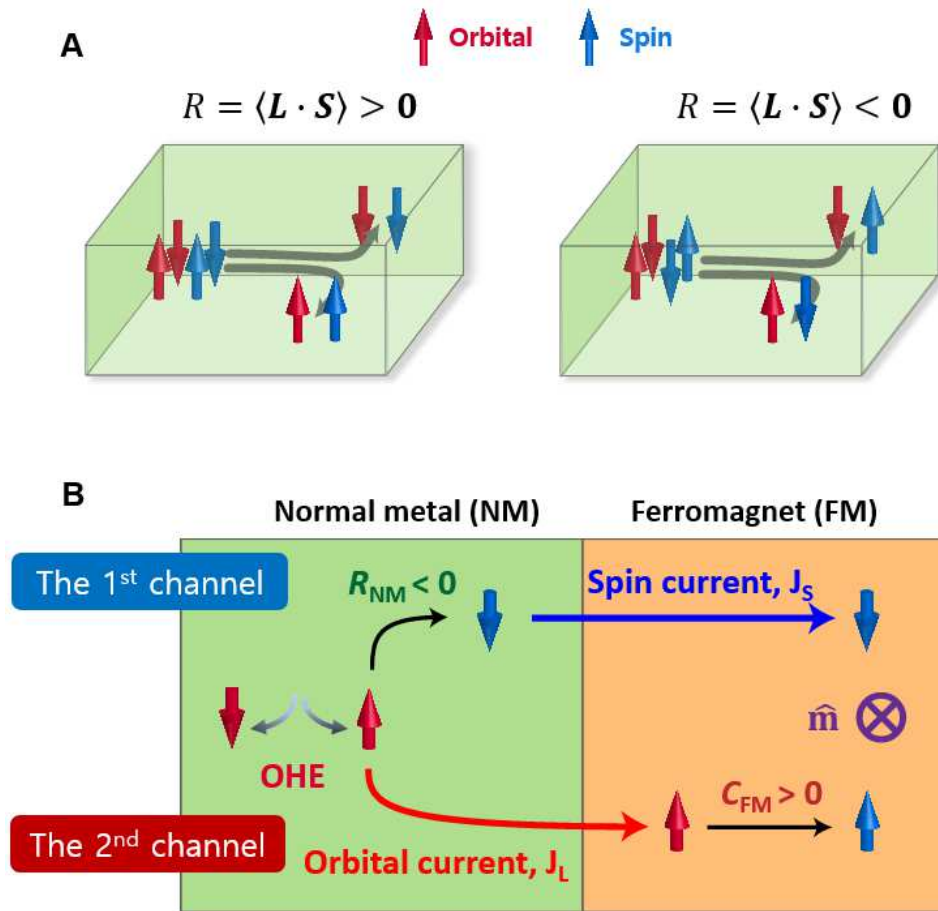


Fig. 1.

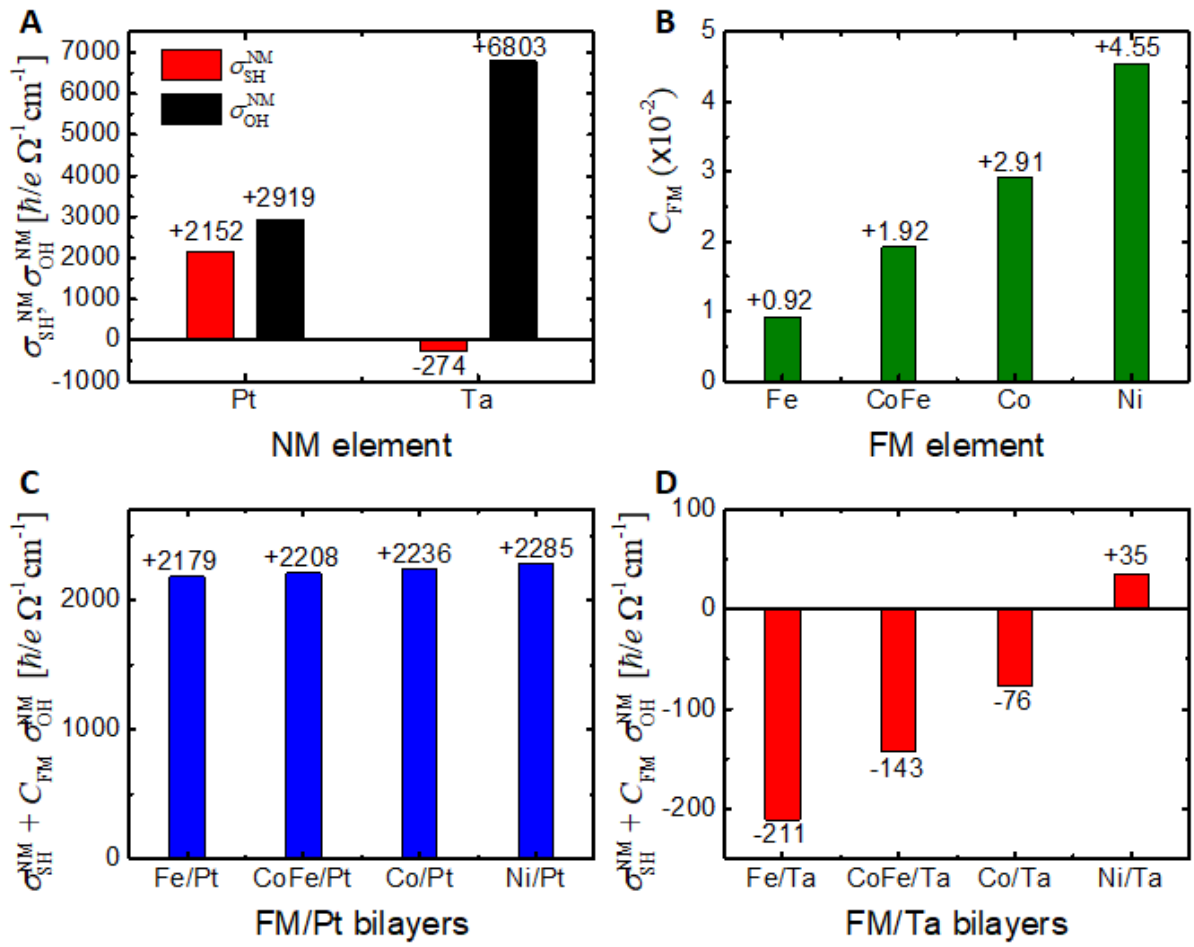


Fig. 2.

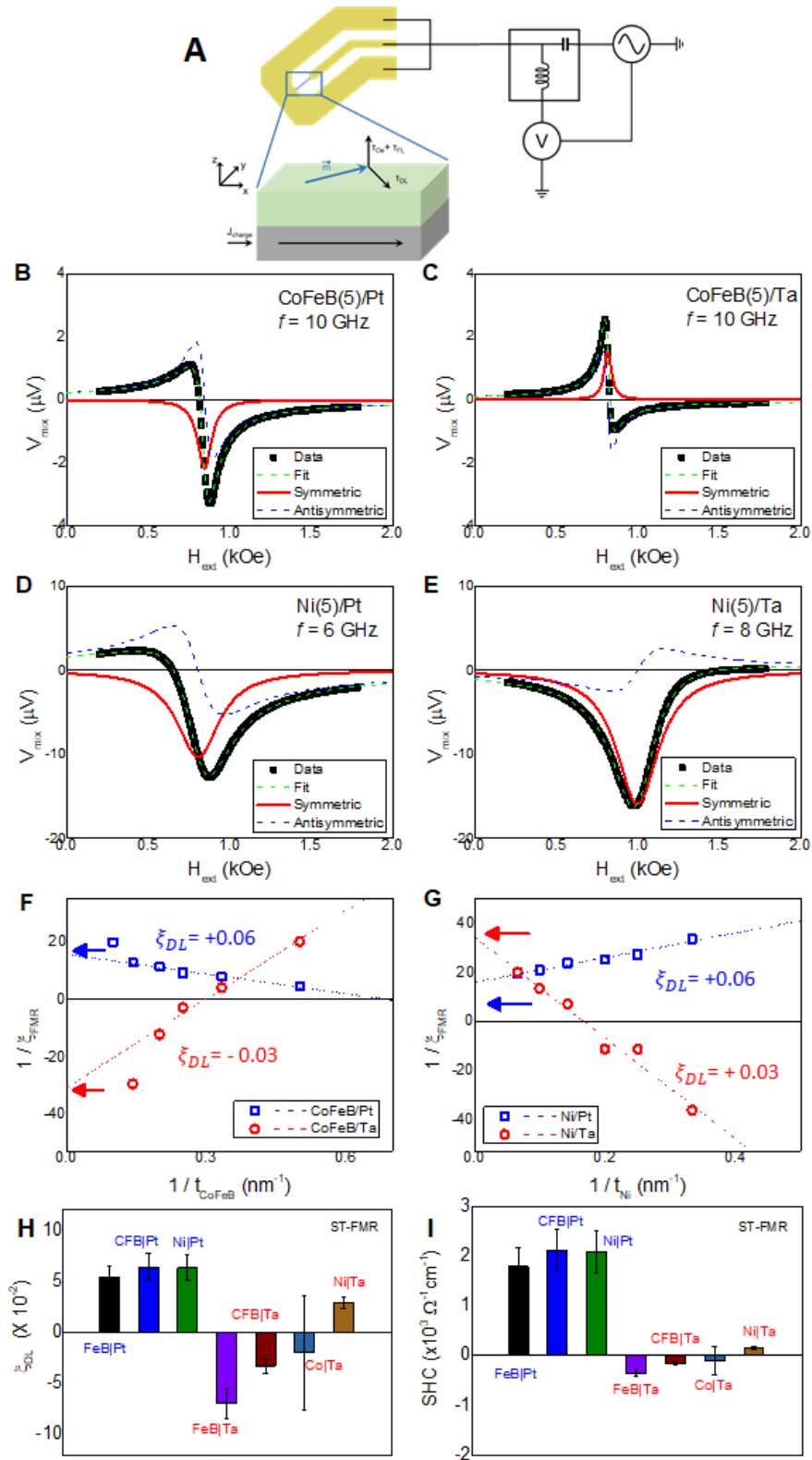


Fig. 3.

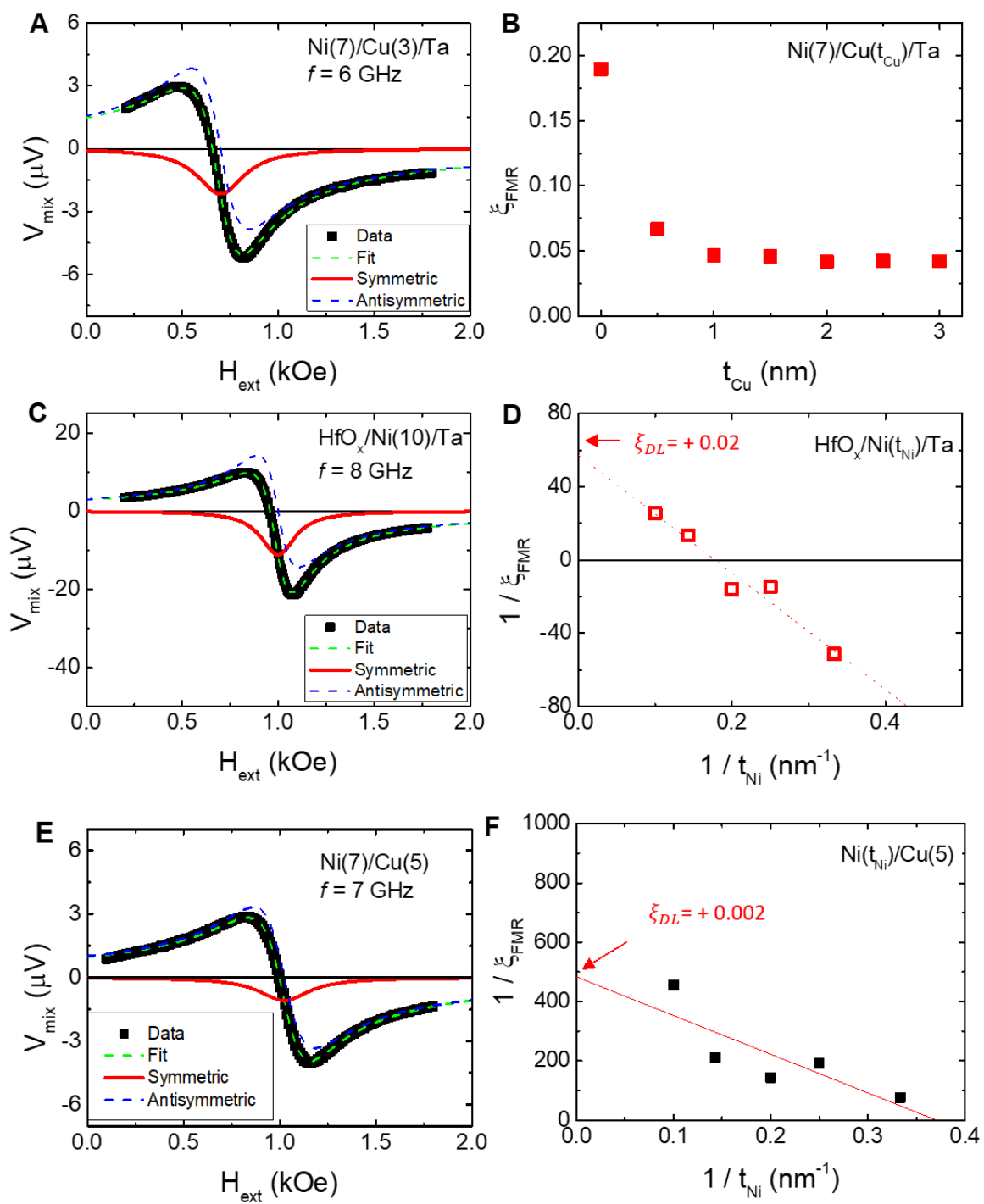


Fig. 4.

REFERENCES

1. D'yakonov M. I., Perel V. I. Possibility of orienting electron spins with current. *JETP Lett* **13**, 467 (1971).
2. Kato Y. K., Myers R. C., Gossard A. C., Awschalom D. D. Observation of the spin Hall effect in semiconductors. *science* **306**, 1910 (2004).
3. Wunderlich J., Kaestner B., Sinova J., Jungwirth T. Experimental observation of the spin-Hall effect in a two-dimensional spin-orbit coupled semiconductor system. *Phys Rev Lett* **94**, 047204 (2005).
4. Engel H.-A., Rashba E. I., Halperin B. I. Theory of spin Hall effects in semiconductors. *In Handbook of Magnetism and Advanced Magnetic Materials, edited by H Kronmüller, and S Parkin, John Wiley and Sons, New York, p. 2858 (2006).*
5. Nozières P., Lewiner C. A simple theory of the anomalous Hall effect in semiconductors. *J Phys France* **34**, 901-915 (1973).
6. Park S. R., Kim C. H., Yu J., Han J. H., Kim C. Orbital-angular-momentum based origin of Rashba-type surface band splitting. *Phys Rev Lett* **107**, 156803 (2011).
7. Go D., Jo D., Kim C., Lee H.-W. Intrinsic Spin and Orbital Hall Effects from Orbital Texture. *Phys Rev Lett* **121**, 086602 (2018).
8. Murakami S., Nagaosa N., Zhang S.-C. Dissipationless quantum spin current at room temperature. *Science* **304**, 1348-1351 (2003).
9. Sinova J., Culcer D., Niu Q., Sinitsyn N. A., Jungwirth T., MacDonald A. H. Universal intrinsic spin Hall effect. *Phys Rev Lett* **92**, 126603 (2004).
10. Tanaka T., Kontani H., Naito M., Naito T., Hirashima D. S., Yamada K., Inoue J. Intrinsic spin Hall effect and orbital Hall effect in 4d and 5d transition metals. *Physical Review B* **77**, 165117 (2008).
11. Kontani H., Tanaka T., Hirashima D. S., Yamada K., Inoue J. Giant orbital Hall effect in transition metals: origin of large spin and anomalous Hall effects. *Phys Rev Lett* **102**, 016601 (2009).
12. Bernevig B. A., Hughes T. L., Zhang S. C. Orbitronics: the intrinsic orbital current in p-doped silicon. *Phys Rev Lett* **95**, 066601 (2005).
13. Haney P. M., Stiles M. D. Current-induced torques in the presence of spin-orbit coupling. *Phys Rev Lett* **105**, 126602 (2010).
14. Hoffmann A. Spin Hall Effects in Metals. *IEEE T Magn* **49**, 5172-5193 (2013).
15. Sinova J., Valenzuela S. O., Wunderlich J., Back C. H., Jungwirth T. Spin Hall Effects. *Rev Mod Phys* **87**, 1213-1259 (2015).
16. Miron I. M., *et al.* Perpendicular Switching of a Single Ferromagnetic Layer Induced

- by In-Plane Current Injection. *Nature* **476**, 189-193 (2011).
17. Liu L. Q., Pai C.-F., Li Y., Tseng H. W., Ralph D. C., Buhrman R. A. Spin torque switching with the giant spin Hall effect of tantalum. *Science* **336**, 555-558 (2012).
 18. Emori S., Bauer U., Ahn S. M., Martinez E., Beach G. S. Current-driven dynamics of chiral ferromagnetic domain walls. *Nat Mater* **12**, 611-616 (2013).
 19. Ryu K. S., Thomas L., Yang S. H., Parkin S. Chiral spin torque at magnetic domain walls. *Nat Nanotechnol* **8**, 527-533 (2013).
 20. Sagasta E., *et al.* Unveiling the mechanisms of the spin Hall effect in Ta. *Physical Review B* **98**, 060410 (2018).
 21. Go D., Lee H.-W. Orbital torque: Torque generation by orbital current injection. *Physical Review Research* **2**, 0131777 (2020).
 22. Kim J., Go D., Tsai H., Jo D., Kondou K., Lee H.-W., Otani Y. Nontrivial torque generation by orbital angular momentum injection in ferromagnetic-metal/Cu/Al₂O₃ trilayers. *Physical Review B* **103**, L020407 (2021).
 23. Ding S., *et al.* Harnessing Orbital-to-Spin Conversion of Interfacial Orbital Currents for Efficient Spin-Orbit Torques. *Phys Rev Lett* **125**, 177201 (2020).
 24. Tazaki T., Kageyama Y., Hayashi H., Harumoto T., Gao T., Shi J., Ando K. Current-induced torque originating from orbital current. *arXiv* **2004**, 09165 (2020).
 25. Go D., Jo D., Gao T., Ando K., Blügel S., Lee H.-W., Mokrousov Y. Orbital Rashba effect in a surface-oxidized Cu film. *Physical Review B* **103**, L121113 (2021).
 26. Guo G. Y., Murakami S., Chen T. W., Nagaosa N. Intrinsic spin Hall effect in platinum: first-principles calculations. *Phys Rev Lett* **100**, 096401 (2008).
 27. Qiao J., Zhou J., Yuan Z., Zhao W. Calculation of intrinsic spin Hall conductivity by Wannier interpolation. *Physical Review B* **98**, 214402 (2018).
 28. Liu L., Moriyama T., Ralph D. C., Buhrman R. A. Spin-Torque Ferromagnetic Resonance Induced by the Spin Hall Effect. *Phys Rev Lett* **106**, 036601 (2011).
 29. Zhang W., Han W., Jiang X., Yang S.-H., Parkin S. S. P. Role of Transparency of Platinum–Ferromagnet Interfaces in Determining the Intrinsic Magnitude of the Spin Hall Effect. *Nat Phys* **11**, 496-502 (2015).
 30. Pai C.-F., Ou Y., Vilela-Leão L. H., Ralph D. C., Buhrman R. A. Dependence of the Efficiency of Spin Hall Torque on the Transparency of Pt/Ferromagnetic Layer Interfaces. *Phys Rev B* **92**, 064426 (2015).
 31. Lee D. J., Kim J. H., Park H. G., Lee K.-J., Ju B.-K., Koo H. C., Min B.-C., Lee O. J. Spin-Orbit Torque and Magnetic Damping in Tailored Ferromagnetic Bilayers. *Phys Rev Appl* **10**, 024029 (2018).

32. Karimeddiny S., Mittelstaedt J. A., Buhrman R. A., Ralph D. C. Transverse and Longitudinal Spin-Torque Ferromagnetic Resonance for Improved Measurement of Spin-Orbit Torque. *Physical Review Applied* **14**, 024024 (2020).
33. Kageyama Y., Tazaki Y., An H., Harumoto T., Gao T., Shi J., Ando K. Spin-orbit torque manipulated by fine-tuning of oxygen-induced orbital hybridization. *Science Advances* **5**, eaax4278 (2019).
34. Wang L., Wesselink R. J., Liu Y., Yuan Z., Xia K., Kelly P. J. Giant Room Temperature Interface Spin Hall and Inverse Spin Hall Effects. *Phys Rev Lett* **116**, 196602 (2016).
35. Baek S. C., *et al.* Spin currents and spin-orbit torques in ferromagnetic trilayers. *Nat Mater* **17**, 509-513 (2018).
36. Amin V. P., Zemen J., Stiles M. D. Interface-Generated Spin Currents. *Phys Rev Lett* **121**, 136805 (2018).
37. Fan X., Celik H., Wu J., Ni C., Lee K. J., Lorenz V. O., Xiao J. Q. Quantifying interface and bulk contributions to spin-orbit torque in magnetic bilayers. *Nat Commun* **5**, 3042 (2014).
38. Krupin O., Bihlmayer G., Starke K., Gorovikov S., Prieto J. E., Döbrich K., Blügel S., Kaindl G. Rashba effect at magnetic metal surfaces. *Physical Review B* **71**, 201403 (2005).
39. Qiu X., *et al.* Spin-Orbit-Torque Engineering via Oxygen Manipulation. *Nat Nanotechnol* **10**, 333-338 (2015).
40. Gurvich L. V., Veyts I. V., Alcock C. B. Thermodynamic properties of individual substances, Fourth Edition, Vol. 3, CRC Press, Boca Raton, FL. (1994).
41. Amin V. P., Li J., Stiles M. D., Haney P. M. Intrinsic Spin Currents in Ferromagnets. *Phys Rev B* **99**, 220405 (2019).
42. Wang W., *et al.* Anomalous Spin-Orbit Torques in Magnetic Single-Layer Films. *Nat Nanotechnol* **14**, 819-824 (2019).
43. Go D., *et al.* Theory of Current-Induced Angular Momentum Transfer Dynamics in Spin-Orbit Coupled Systems. *Phys Rev Res* **2**, 033401 (2020).
44. Jo D., Go D., Lee H.-W. Gigantic intrinsic orbital Hall effects in weakly spin-orbit coupled metals. *Physical Review B* **98**, 214405 (2018).
45. Parkin S. S., Kaiser C., Panchula A., Rice P. M., Hughes B., Samant M., Yang S. H. Giant tunnelling magnetoresistance at room temperature with MgO (100) tunnel barriers. *Nat Mater* **3**, 862-867 (2004).
46. Yuasa S., Nagahama T., Fukushima A., Suzuki Y., Ando K. Giant room-temperature magnetoresistance in single-crystal Fe/MgO/Fe magnetic tunnel junctions. *Nat Mater* **3**, 868-871 (2004).

47. Butler W. H., Zhang X. G., Schulthess T. C., MacLaren J. M. Spin-dependent tunneling conductance of Fe|MgO|Fe sandwiches. *Physical Review B* **63**, 054416 (2001).
48. Mathon J., Umerski A. Theory of tunneling magnetoresistance of an epitaxial Fe/MgO/Fe(001) junction. *Physical Review B* **63**, 220403 (2001).
49. Rau I. G., *et al.* Reaching the magnetic anisotropy limit of a 3d metal atom. *Science* **344**, 988-992 (2014).
50. Sunko V., *et al.* Maximal Rashba-like spin splitting via kinetic-energy-coupled inversion-symmetry breaking. *Nature* **549**, 492-496 (2017).
51. Okada A., Takeuchi Y., Furuya K., Zhang C., Sato H., Fukami S., Ohno H. Spin-Pumping-Free Determination of Spin-Orbit Torque Efficiency from Spin-Torque Ferromagnetic Resonance. *Physical Review Applied* **12**, 014040 (2019).

Supplementary Files

This is a list of supplementary files associated with this preprint. Click to download.

- [20210509OTsupplementaryNCOMM.docx](#)